Results in Physics 57 (2024) 107410

Contents lists available at ScienceDirect

Results in Physics

journal homepage: www.elsevier.com/locate/rinp

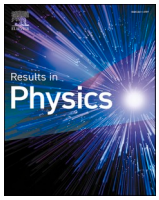

Impact of the magnetic field and the height and number of triangular blades inside a rectangular cavity on natural convection heat transfer

Jawed Mustafa [a,*], Saeed Alqaed [a], S. Mohammad Sajadi [b], Abdulrahman Mohammed Alsaiari [c], Hikmet Ş. Aybar [d,e,*]

[a] Mechanical Engineering Department, College of Engineering, Najran University, P.O. Box (1988), Najran 61441, Saudi Arabia
[b] Department of Nutrition, Cihan University-Erbil, Kurdistan Region, Iraq
[c] Department Architecture Engineering, College of Engineering, Najran University, P.O. Box (1988), Najran, 61441, Saudi Arabia
[d] Department of Mechanical Engineering, Eastern Mediterranean University, Famagusta, TRNC, via Mersin 10, Turkey
[e] Department of Medical Research, China Medical University Hospital, China Medical University, Taichung, Taiwan

ARTICLE INFO

Keywords:
Magnetic field
Blade
Nanofluid
Numerical methods
Nusselt number

ABSTRACT

In this article, the effect of the blades placed in a cavity on the natural flow of alumina/water nanofluid is examined. The cavity has two insulated walls, a cold wall at the top, and a hot wall at the bottom affected by a magnetic field. The triangular blades at the same temperature at the bottom wall are placed on the wall. For the simulations, the Lattice Boltzmann Method (LBM) is used. The findings show that the average Nusselt number (Nu-Av) increases by more than 96 % when the dimensionless length of the blades (L-B) is raised from 0.3 to 0.7 for the case of 3 blades. With the initial increase in the L-Bs, the Nu is increased. The L-B of 0.4 and the highest value of the Nu-Av are equivalent. As the L-Bs is enhanced, the Nu is decreased. At Ra = 10^3, the enhancement in the number of blades (N-Bs) causes an increment in heat transfer (HTR), but at Ra = 10^5, maximum HTR occurs when the N-Bs is 2, and enhancing the N-Bs causes a decrease in HTR.

Introduction

By employing well-liked numerical approaches including the Finite Volume Method (FVM), Finite Element Method (FEM), and Finite Difference Method (FDM), researchers have simulated heat transport concerns by solving the Navier-Stokes and energy equations [1–3]. However, there are several problems with numerical simulations due to the different material properties at the level of heat exchange between the solid and fluid boundary [4–6]. Researchers have also found it difficult to accurately apply the boundary criteria of mixed heat transfer in complicated geometries [7].

To address these issues, many strategies have been put forward. One of them is LBM [8]. Four models—the BGK, MRT, entropic, and regularized—are used in the LBM, which are based on the kinetic theory of particles. This model has recently undergone rapid development in science and engineering and is now being used as a potent tool for simulating complex issues like combustion and multiphase flows. LBM is a CFD technique used for simulating fluid flow. Instead of solving the Navier-Stokes equations, the LBM employs a discretized Boltzmann equation. In the LBM model, the fluid is represented by imaginary particles undergoing two steps: collision and propagation. LBM offers various advantages over traditional CFD methods, especially when dealing with complex boundaries and microscale environments [9–11]. It includes algorithm parallelization techniques. The LBM has advantages over other numerical techniques due to its mesoscopic scale foundation, including parallel programming, application of simpler boundary conditions, faster processing times, and ease of modeling complex geometries [12–14]. Lai et al. [15] utilized the Lattice Boltzmann Method (LBM) to conduct a numerical evaluation of flow patterns and heat transfer rates (HTR) on a pore scale within a partially filled rectangular channel containing a porous medium. The simulation results facilitated the establishment of a correlation connecting the Nusselt number (Nu) with fluid flow characteristics near the porous medium and the intrinsic properties of the porous material. LBM was used by Zhang et al. [16] to simulate the mixed convection of a copper/water nanofluid within a square chamber with an inclination. The results show that when Ra increases, the isothermal lines' gradients diminish and the temperature distribution becomes more uniform, which causes the Nu on the

* Corresponding authors at: Mechanical Engineering Department, College of Engineering, Najran University, Najran, Saudi Arabia (J. Mustafa) and Department of Mechanical Engineering, Eastern Mediterranean University, Famagusta, TRNC, via Mersin 10, Turkey (Hikmet Ş. Aybar).
E-mail addresses: jmmustafa@nu.edu.sa (J. Mustafa), hikmet.aybar@emu.edu.tr (H.Ş. Aybar).

https://doi.org/10.1016/j.rinp.2024.107410
Received 5 November 2023; Received in revised form 17 January 2024; Accepted 25 January 2024
Available online 1 February 2024
2211-3797/© 2024 The Author(s). Published by Elsevier B.V. This is an open access article under the CC BY license (http://creativecommons.org/licenses/by/4.0/).

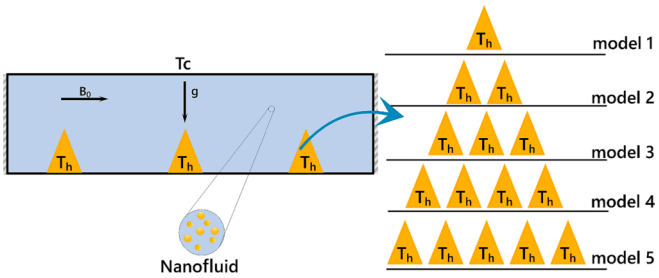

Fig. 1. The geometry of the cavity with different blades.

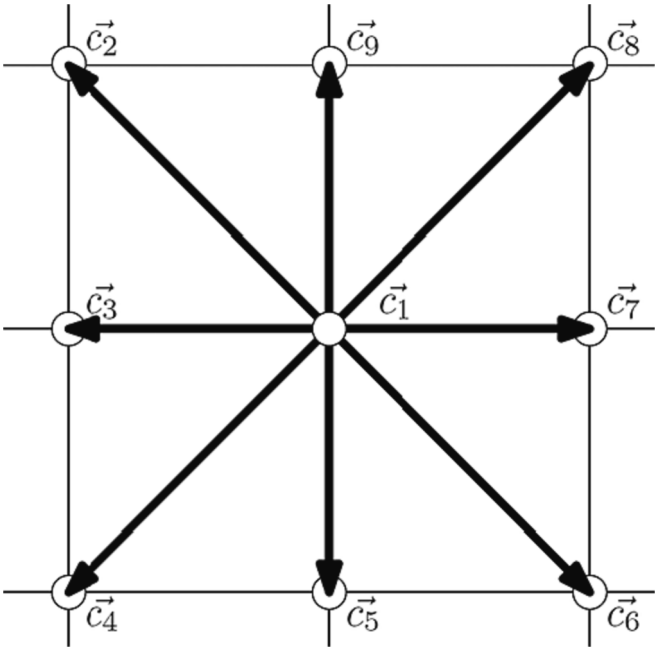

Fig. 2. Discretized velocity vectors for the D2Q9 model.

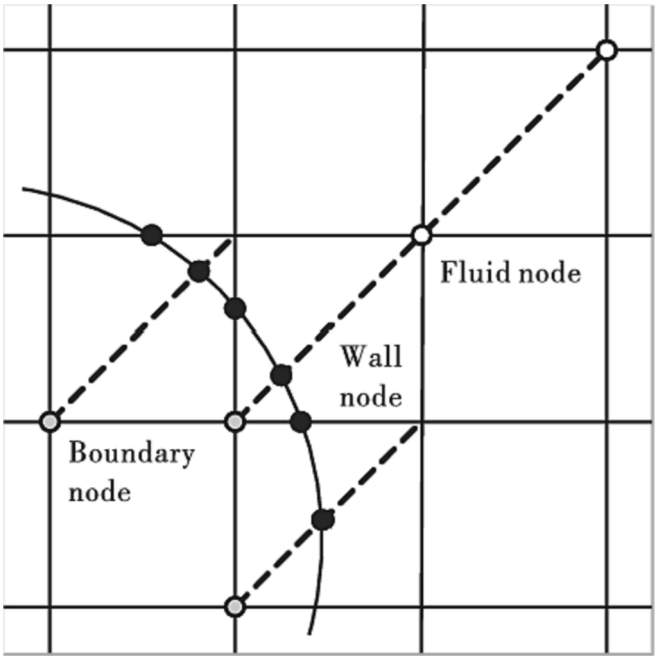

Fig. 3. Grid and boundary of the curved wall configuration.

hot wall to fall. The enhanced HTR was also shown to occur when the heated obstruction is positioned in the flow route. The use of such studies shown their significance in the design of solar energy storage, heat exchangers, lubrication systems, and cooling systems for electronic components. Using the LBM and the Graphical Processing Unit, Yuki et al. [17] evaluated how a magnetic field affected a non-Newtonian power-law nanofluid's natural convection in a rectangular cavity (GPU). A numerical analysis of the effects of magnetic fields on streamlines, isotherms, temperature distribution, and local and Nu-Av for shear-thickening and shear-thinning nanofluids was provided. According to the findings, fluids that thin under shear (n 1) have a higher rate of HTR, while fluids that thicken under shear ($n > 1$) have a lower rate. Di Ilio et al. [18] conducted an extensive numerical exploration of laminar nanofluid flow behavior within channels characterized by undulating walls. They numerically formulated the lattice Boltzmann method (LBM) on an unstructured grid employing a finite volume approach. The findings revealed an enhancement in heat transfer rate (HTR) with increasing amplitude of the undulating surface. However, the Nusselt number averaged along the channel exhibited a decline due to the phase shift between the undulating walls. Notably, the introduction of solid nanoparticles into the base fluid led to a significant augmentation in HTR, particularly with a substantial volume percentage of nanoparticles.

Some studies suggested that employing nanofluids within a symmetrical configuration of a high-amplitude undulating-wall channel could be a promising approach for boosting the thermal efficiency of HTR systems [19]. Moreover, the study alluded to the use of blades in diverse heat exchange devices as a method to expand the heat exchange surface and enhance HTR [20–22]. Closed cavities are one of the heat exchangers used in the industry [23]. Several studies have been conducted on this sort of heat exchanger since it relies on free convection HTR. Nanofluids have been employed in cavities in several studies and researchers in the field of HTR have used nanofluids as one of the applications of nanotechnology for enhancing the efficiency of thermal systems [24–26]. These heat exchangers have various applications, including cooling electronic components, solar panels, enhancing heat transfer in industrial furnaces, direct-absorption solar collectors, and so on.

In this work, using LBM, the influence of geometrical modifications of triangular blades employed in the cavity with the natural flow of a nanofluid is explored in light of the significance of nanofluids in HTR. When the cavity is situated close to the magnetic field and the effect of the N-Bs, the height of the blades is assessed for two Rayleigh numbers. In summary, the utilization of triangular obstacles and variations in their dimensions under boundary conditions is considered an innovative aspect of the paper using LBM.

Problem description

Fig. 1 depicts the cavity's geometry Alumina/water nanofluid is put within the rectangular cavity, which has a length-to-width ratio of around one-third. To the cavity, a horizontal magnetic field with a 20 Hartmann number is applied. At a dimensionless temperature of 0, the upper wall feels cold, while at a dimensionless temperature of 1, the lower wall is perceived as warm. The two side walls are subject to a boundary condition where the temperature gradient $\partial T/\partial x$ is equal to zero. Triangular blades are affixed to the lower wall, ensuring they maintain an identical temperature to that of the wall surface. The investigation involves varying the N-Bs from 1 to 5 and adjusting their height (L) from 0.3 to 0.7 in the scenario of three blades.

Lattice boltzmann approach

The fundamental equation in consideration is the Boltzmann equation [27].

Table 1
Boundary conditions for solving the equations.

Top wall	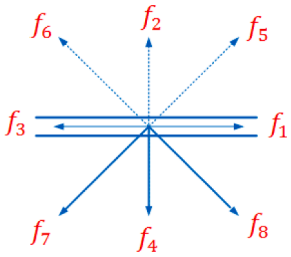	$f_7 = f_5 + 0.5(f_1 - f_3) - \frac{1}{6}\rho_N v_N - 0.5\rho_N u_N f_4 = f_2 - \frac{2}{3}\rho_N v_N f_8 = f_6 + 0.5(f_3 - f_1) - \frac{1}{6}\rho_N v_N + 0.5\rho_N u_N \rho_N = \frac{1}{1+v_N}\{f_0 + f_2 + f_3 + 2(f_2 + f_6 + f_5)\}$	Cold wall $\begin{cases} g_7 = (T_c(w_5 + w_7)) - g_5 \\ g_4 = (T_c(w_2 + w_4)) - g_2 \\ g_8 = (T_c(w_8 + w_6)) - g_6 \end{cases}$
Bottom wall	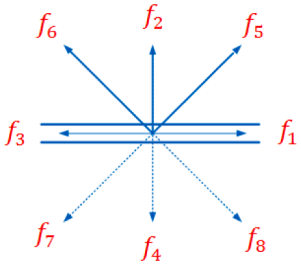	$f_6 = f_8, f_2 = f_4, f_5 = f_7$	Hot walls $\begin{cases} g_5 = (T_h(w_5 + w_7)) - g_7 \\ g_2 = (T_h(w_2 + w_4)) - g_4 \\ g_6 = (T_h(w_8 + w_6)) - g_8 \end{cases}$
Left wall	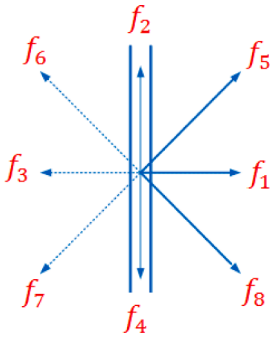	$f_3 = f_1, f_6 = f_8, f_7 = f_5$	Insulated walls $\begin{cases} g_6 = g_5 \\ g_3 = g_1 \\ g_7 = g_8 \end{cases}$
Right wall	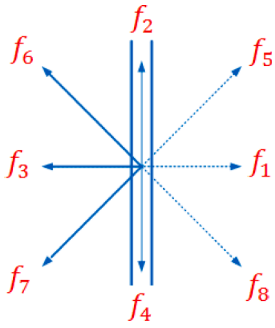	$f_6 = f_8, f_3 = f_1, f_7 = f_5$	Insulated walls $\begin{cases} g_6 = g_5 \\ g_3 = g_1 \\ g_7 = g_8 \end{cases}$

$$f_i\left(\vec{x} + \vec{C}_i\Delta t,\ t + \Delta t\right) = f_i(\vec{x}, t) - \frac{\Delta t}{\tau_\vartheta}\left[(f_i(\vec{x}, t) - f_i^{eq}(\vec{x}, t)\right] \tag{1}$$

The D2Q9 scheme represents the prevalent two-dimensional model employed in the current investigation. Within this framework, eight permissible motion directions are present, as illustrated in Fig. 2. The expression for the vector $\vec{C}_i$ is given by the following equation, where C represents the velocity of virtual particles on the grid [27].

$$\begin{cases} \vec{c_i} = 0\ , & i = 0 \\ \vec{c_i} = C(\cos\theta_i, \sin\theta_i)\ , & \theta_i = (i-1)\pi/2\ , & i = 1,2,3,4 \\ \vec{c_i} = C\sqrt{2}\,(\cos\theta_i,\ \sin\theta_i)\ , & \theta_i = \left(i-5\right)\pi\Big/2 + \pi\Big/4\ , & i = 5,6,7,8 \end{cases} \tag{2}$$

The subsequent description presents an alternative characterization for the equilibrium distribution function [27].

$$f_i^{(eq)} = \omega_i\rho\left[1 + 3\frac{\vec{c_i}\cdot\vec{u}}{C^2} + \frac{9}{2}\frac{(\vec{c_i}\cdot\vec{u})^2}{C^4} - \frac{3}{2}\frac{\vec{u}^2}{C^2}\right] \tag{3}$$

where ω_i is

Table 2
Thermophysical properties of water and Al_2O_3 [36].

	$k\,(W/m.K)$	$\rho\,(kg/m^3)$	$\mu\,(kg/m.s)$	$C_P\,(J/kg.K)$
Water	0.613	997.1	0.001	4179
Al_2O_3	40	3970	–	765

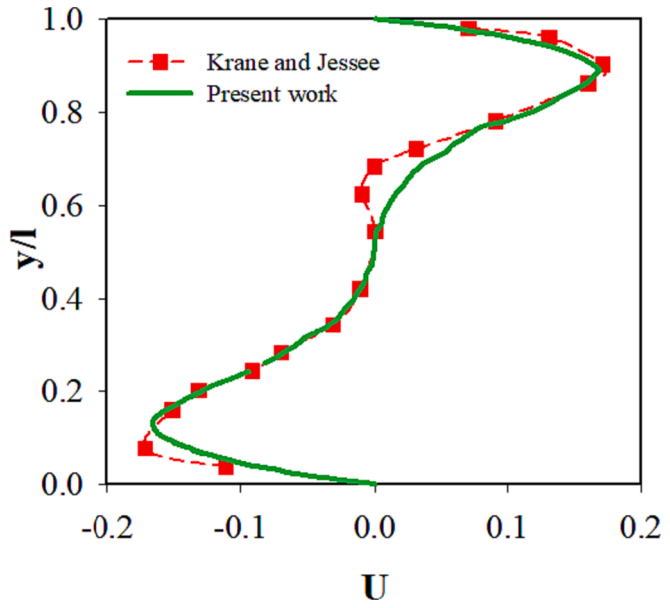

Fig. 4. Comparison between the dimensionless horizontal velocity along the cavity's central axis in the present study and the results reported in Reference [37].

Table 3
Comparison of the maximum vorticity power and average Nusselt number between the present work and the study by Vahedi et al. [38].

	This work	Vahedi et al. [38]	Error
Nu-Av	2.596	2.716	4.41 %
ψ	4.612	4.777	3.45 %

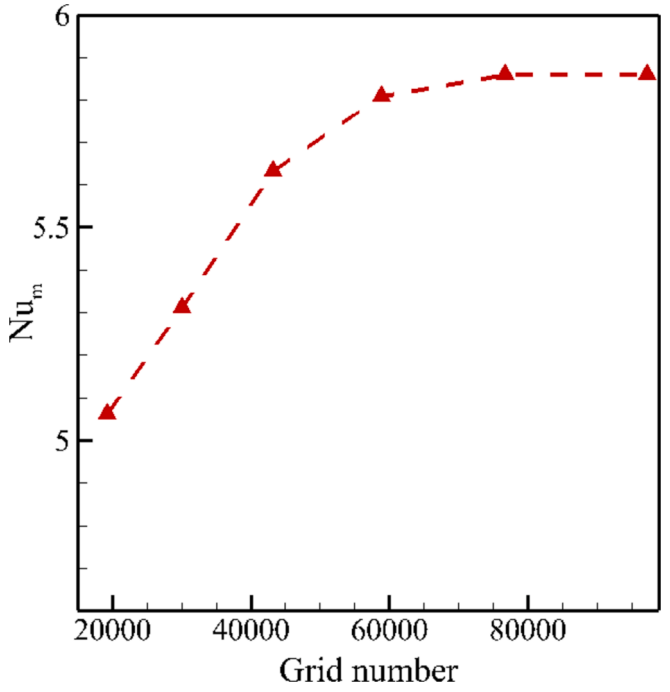

Fig. 5. Impact of varying the number of grid points on the Nu-Av.

$$\omega_i = \begin{cases} \frac{4}{9}, & i = 0 \\ \frac{1}{9}, & i = 1,2,3,4 \\ \frac{1}{36}, & i = 5,6,7,8 \end{cases} \tag{4}$$

The kinematic viscosity (ϑ) and relaxation time (τ_ϑ) are linked [27]:

$$\vartheta = C_s^2 \Delta t(\tau_\vartheta - 0.5) \tag{5}$$

Here, $c_s = c/\sqrt{3}$ is the speed of sound [28].

Calculations for macroscopic characteristics like fluid density and velocity look like this [27]:

$$\rho = \sum_{i=0}^{8} f_i \tag{6}$$

$$\rho \vec{u} = \sum_{i=0}^{8} \vec{c}_i f_i \tag{7}$$

The collision and diffusion stages are represented as

$$\widetilde{f}_i(\vec{x}, t + \Delta t) = f_i(\vec{x}, t) - \frac{\Delta t}{\tau_\vartheta}\left[(f_i(\vec{x}, t) - f_i^{eq}(\vec{x}, t)\right] \tag{8}$$

$$f_i\left(\vec{x} + \vec{c}_i \Delta t, t + \Delta t\right) = \widetilde{f}_i(\vec{x}, t + \Delta t) \tag{9}$$

In the context of free convective heat transfer scenarios, the dominating external force corresponds to the buoyancy force. Hence [27]:

$$f_i\left(\vec{x} + \vec{c}_i \Delta t,\ t + \Delta t\right) = f_i(\vec{x}, t) - \frac{\Delta t}{\tau_\vartheta}\left[(f_i(\vec{x}, t) - f_i^{eq}(\vec{x}, t)\right] + \Delta t F_i(\vec{x}, t) \bullet \frac{\vec{c}_i}{C_s^2} \tag{10}$$

The Boussinesq approximation is used to determine the buoyancy force. Thus [27]:

$$\begin{aligned} F_x &= w_i \rho \left[\frac{Ha^2 \mu}{H^2}\left(v sin(\gamma) cos(\gamma) - \left(u sin^2(\gamma)\right)\right)\right] \\ F_y &= w_i \rho \left[\frac{Ha^2 \mu}{H^2}\left(u \sin(\gamma) cos(\gamma) - v \cos^2(\gamma)\right) + g_y \beta\left(T\left(\vec{x}, t\right) - T_\infty\right)\right] \end{aligned} \tag{11}$$

Viscous dissipation is neglected. Here is the energy equation as it appears within the lattice Boltzmann method [27]:

$$g_i\left(\vec{x} + \vec{C}_i \Delta t,\ t + \Delta t\right) = g_i(\vec{x}, t) - \frac{\Delta t}{\tau_T}\left[(g_i(\vec{x}, t) - g_i^{eq}(\vec{x}, t)\right] \tag{12}$$

Represented by g_i, the energy distribution function along the discretized velocity i is denoted. The equilibrium energy distribution function and the macroscopic temperature are subsequently expressed as follows [27]:

$$g_i^{(eq)} = \omega_i T\left[1 + 3\frac{\vec{c}_i \cdot \vec{u}}{C^2} + \frac{9}{2}\frac{(\vec{c}_i \cdot \vec{u})^2}{C^4} - \frac{3}{2}\frac{\vec{u}^2}{C^2}\right] \tag{13}$$

$$T = \sum_{i=0}^{8} g_i \tag{14}$$

The expression for the thermal diffusion coefficient is given by:

$$\alpha = C_s^2 \Delta t(\tau_T - 0.5) \tag{15}$$

The dimensionless parameters of the problem are

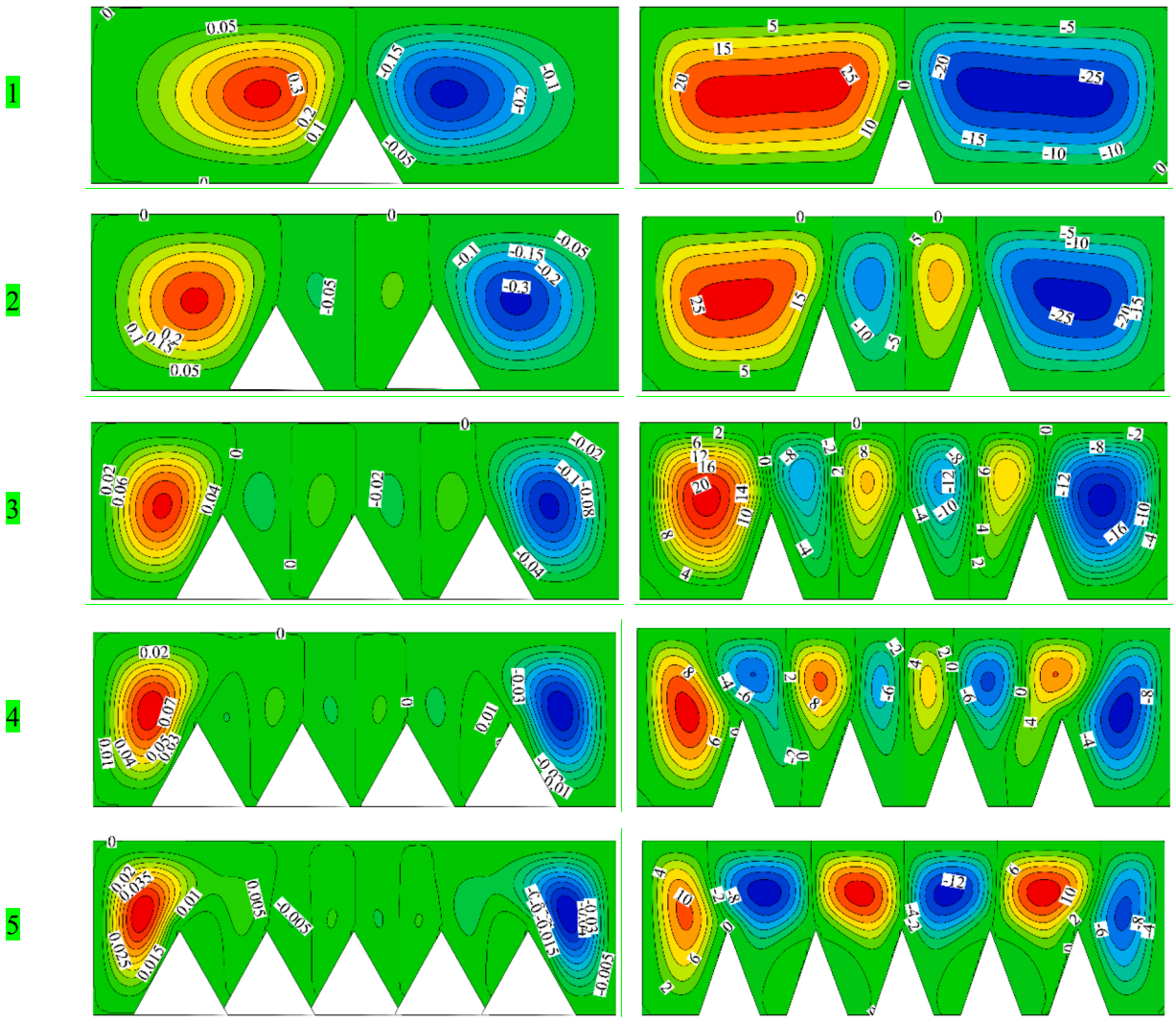

Fig. 6. Flow contours for two different values of Ra (10^3 and 10^5) and the various N-Bs (1to5 blade).

$$X^* = \frac{x}{W}, Y^* = \frac{y}{W}, U = \frac{uW}{\alpha_f}, V = \frac{vW}{\alpha_f}$$
$$\alpha^* = \frac{\alpha_{nf}}{\alpha_f}, \mu = \frac{\mu_{nf}}{\mu_f}, k = \frac{k_{nf}}{k_f}, \theta = \frac{T - T_C}{\Delta T} \quad (16)$$
$$Pr = \frac{\vartheta}{\alpha}, Ra = \frac{g_y \beta H^3 \Delta T}{\vartheta \alpha}, Ha = HB_0\sqrt{\frac{\sigma}{\mu}}$$

The boundary conditions are stated as follows:

Bottom wall and blades:

$$U = V = 0,\ \theta = 1 \quad (17)$$

Top wall:

$$U = V = 0, \theta = 0 \quad (18)$$

Side walls

$$U = V = 0, \frac{\partial \theta}{\partial x} = 0 \quad (19)$$

Fig. 3 [29] is used to compute the temperature and velocity on the curved border.

The boundary conditions for incorporation into the lattice Boltzmann equations are presented in Table 1.

On the boundaries of the curve, the methods proposed by Mi et al. [30] and Jo et al. [31] have been applied. Fig. 3 provides an illustration of the curve boundary and the nodal network. Nodes existing in the solid boundary region are denoted with a subscript "b." The intersection point of the curve boundary with the grid is specifically identified with a subscript "w." Moreover, the first and second nodes along each axis of the network within the computational domain are respectively designated with subscripts "f" and "ff." Additionally, the parameter Δ, used for calculating density and energy distribution functions after collisions, is expressed by the following equation.

$$\Delta = \left| \frac{\vec{x}_f - \vec{x}_w}{\vec{x}_f - \vec{x}_b} \right| \quad (20)$$

To implement the dispersion stage on the fluid nodes in the vicinity of the curve boundary, it is necessary to compute $\widetilde{f}_{\bar{\alpha}}(\vec{x}_b, t)$ and $\widetilde{g}_{\bar{\alpha}}(\vec{x}_b, t)$, where $\vec{e}_{\bar{\alpha}} = -\vec{e}_\alpha$. The computation of these functions is performed using information from the curve boundary and solid boundary nodes:

$$\widetilde{f}_{\bar{\alpha}}\left(\vec{x}_b, t\right) = (1-\chi)\widetilde{f}_{\bar{\alpha}}\left(\vec{x}_f, t\right) + \chi f_\alpha^*\left(\vec{x}_b, t\right) - 2\omega_\alpha \rho\left(\vec{x}_f, t\right) \bullet \frac{3}{C^2}\vec{e}_\alpha . \vec{u}_w \quad (21)$$

$$f_\alpha^*\left(\vec{x}_b, t\right) = f_\alpha^{eq}\left(\vec{x}_f, t\right) + \omega_\alpha \rho\left(\vec{x}_f, t\right) \bullet \frac{3}{C^2}\vec{e}_\alpha . \left(\vec{u}_{bf} - \vec{u}_f\right) \quad (22)$$

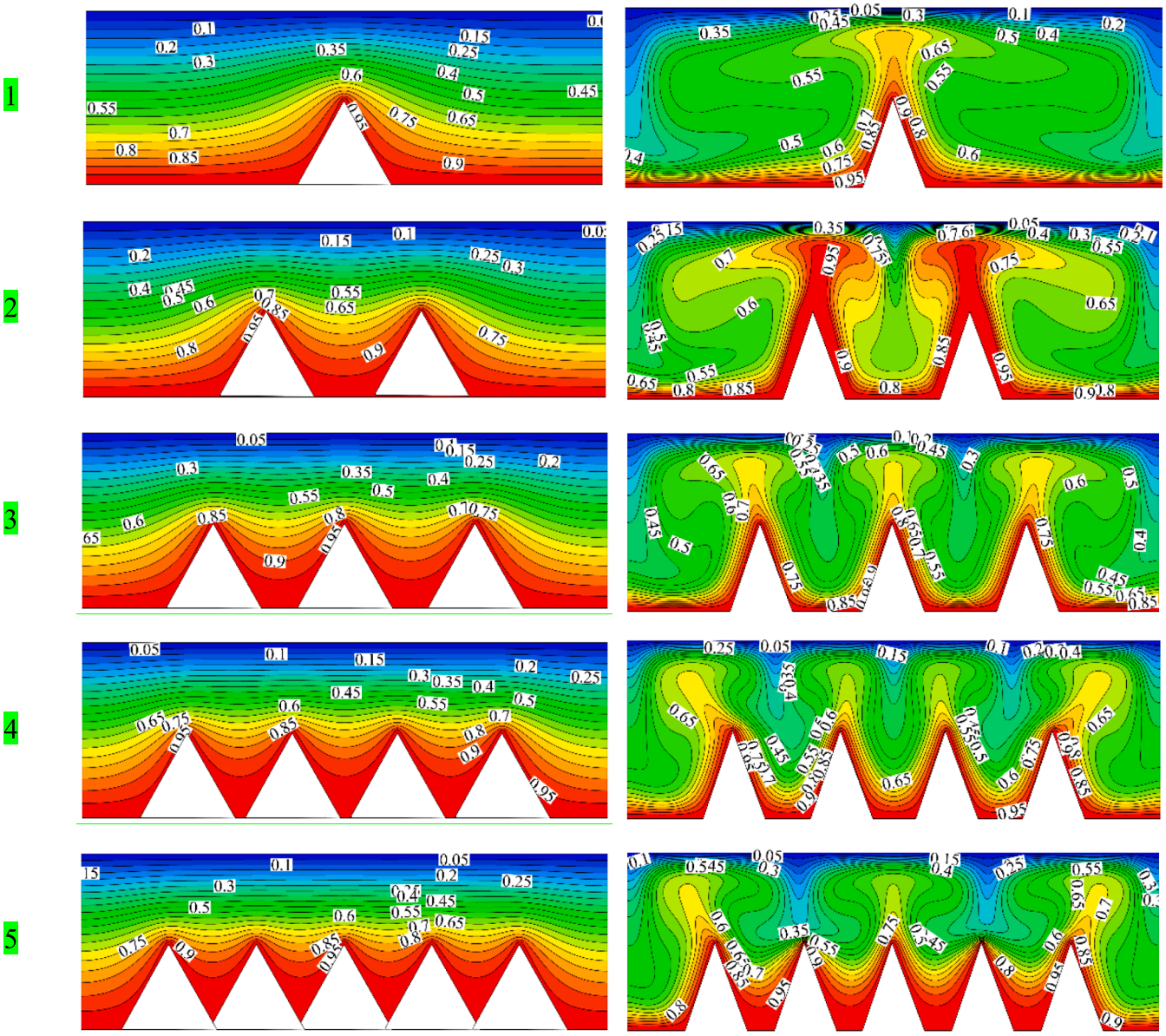

Fig. 7. Temperature contours for two different values of Ra (10^3 and 10^5) and the various N-Bs (1to5 blade).

Mi et al. [30] proposed the following expressions to calculate the weighting factor χ and the virtual velocity $\vec{u}_{bf}$: (23)

$$\vec{u}_{bf} = \vec{u}_{ff} = \vec{u}\left(\vec{x}_{ff}, t\right), \chi = \frac{(2\Delta - 1)}{\tau - 2}, 0 < \Delta \le \frac{1}{2} \tag{23}$$

$$\vec{u}_{bf} = \vec{u}_f + \frac{3}{2\Delta}\left(\vec{u}_w - \vec{u}_f\right), \chi = \frac{(2\Delta - 1)}{\tau - 0.5}, \frac{1}{2} < \Delta \le 1 \tag{24}$$

For the energy distribution function, the proposed relations by Jo et al. [31] are utilized:

$$\tilde{g}_{\bar{\alpha}}\left(\vec{x}_b, t + \Delta t\right) = \tilde{g}^{eq}_{\bar{\alpha}}\left(\vec{x}_b, t\right) + \left(1 - \frac{1}{\tau_T}\right)\tilde{g}^{neq}_{\bar{\alpha}}\left(\vec{x}_b, t\right) \tag{25}$$

$$\tilde{g}^{eq}_{\bar{\alpha}}\left(\vec{x}_b, t\right) = \omega_{\bar{\alpha}} T_b^{*}\left(1 + \frac{3}{C^2}\vec{e}_{\bar{\alpha}}.\vec{u}_b^{\,*}\right) \tag{26}$$

$$\tilde{g}^{neq}_{\bar{\alpha}}\left(\vec{x}_b, t\right) = \Delta g^{neq}_{\bar{\alpha}}\left(\vec{x}_f, t\right) + (1 - \Delta) g^{neq}_{\bar{\alpha}}\left(\vec{x}_{ff}, t\right) \tag{27}$$

In the above equations, the unknown values and parameters are obtained as follows:

$$\vec{u}_b^{\,*} = \vec{u}_{b1}\ ,\ \Delta > 0.75 \tag{28}$$

$$\vec{u}_b^{\,*} = \vec{u}_{b1} + (1 - \Delta)\vec{u}_{b2}\ ,\ \Delta \le 0.75 \tag{29}$$

$$T_b^{*} = T_{b1}\ ,\ \Delta > 0.75 \tag{30}$$

$$T_b^{*} = T_{b1} + (1 - \Delta)T_{b2}\ ,\ \Delta \le 0.75 \tag{31}$$

$$\vec{u}_{b1} = \frac{1}{\Delta}\left(\vec{u}_w + (\Delta - 1)\vec{u}_f\right) \tag{32}$$

$$\vec{u}_{b2} = \frac{1}{\Delta + 1}\left(2\vec{u}_w + (\Delta - 1)\vec{u}_{ff}\right) \tag{33}$$

$$\vec{T}_{b1} = \frac{1}{\Delta}\left(T_w + (\Delta - 1)T_f\right) \tag{34}$$

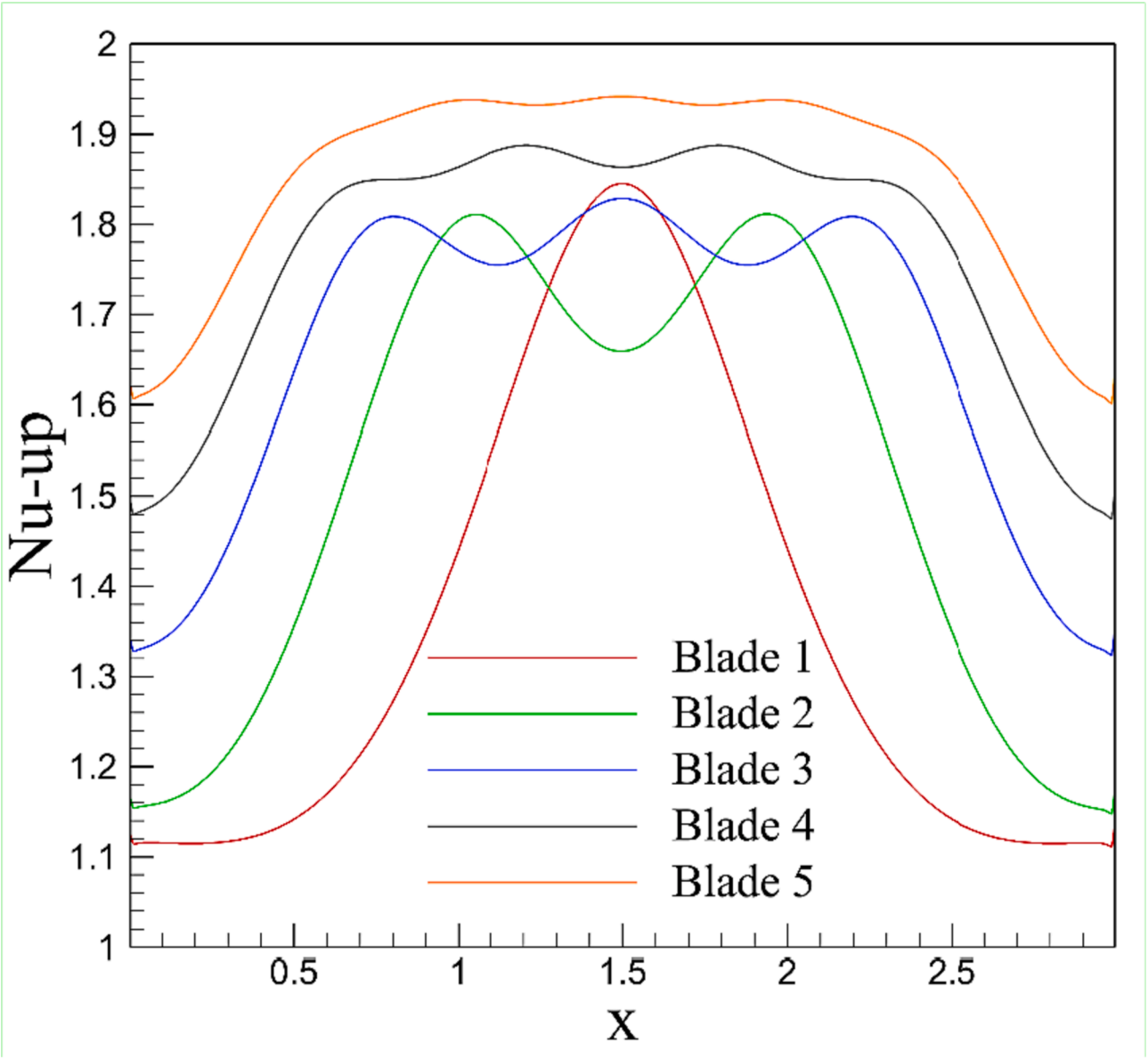

Fig. 8. Local Nu on the top wall for different numbers of blades (1to5 blade) at Ra = 1000.

$$\overrightarrow{T}_{b2} = \frac{1}{\Delta + 1}\left(2T_w + (\Delta - 1)T_{ff}\right) \tag{35}$$

Local and Nu-Av are defined as.

$$Nu_L = -\frac{k_{nf}}{k_f}\left(\frac{\partial\theta}{\partial X}\right) \tag{36}$$

$$Nu - Av = \frac{1}{L}\int_0^L Nu_L d\eta \tag{37}$$

Governing equations for nanofluid

The nanofluid properties are as follows [32].

$$\rho_{nf} = (1-\varphi)\rho_f + \varphi\rho_p \tag{38}$$

$$(C_P)_{nf} = \left[\frac{1}{1+\frac{(1-\varphi)\rho_f}{\varphi\rho_p}}\frac{(c_P)_p}{(c_P)_f} + \frac{1}{1+\frac{\varphi\rho_p}{(1-\varphi)\rho_f}}\right](c_P)_{nf} \tag{39}$$

$$\beta_{nf} = \left[\frac{1}{1+\frac{(1-\varphi)\rho_f}{\varphi\rho_p}}\frac{\beta_p}{\beta_f} + \frac{1}{1+\frac{\varphi\rho_p}{(1-\varphi)\rho_f}}\right]\beta_f \tag{40}$$

In all equations related to nanofluid, the subscript "f" is used for the fluid, "nf" for the nanofluid, and "p" for nanoparticles. Additionally, c_P and β represent density, specific heat capacity, and volumetric expansion coefficient, respectively. In the above equations, by substituting φ, which represents the volume fraction of nanoparticles, the values are calculated.

For nanofluid viscosity [33] is used, while for nanofluid thermal conductivity Maxwell [34] Vajjha [35] is used.

$$\mu_{nf} = \frac{\mu_f}{(1-\varphi)^{2.5}} + 5 \times 10^4\left(8.4407(100\varphi)^{-1.07304}\right)\varphi\rho_f(c_p)_f\frac{\mu_f}{k_f pr}\sqrt{\frac{k_b T}{\rho_p d_p}}f\left(T,\varphi\right) \tag{41}$$

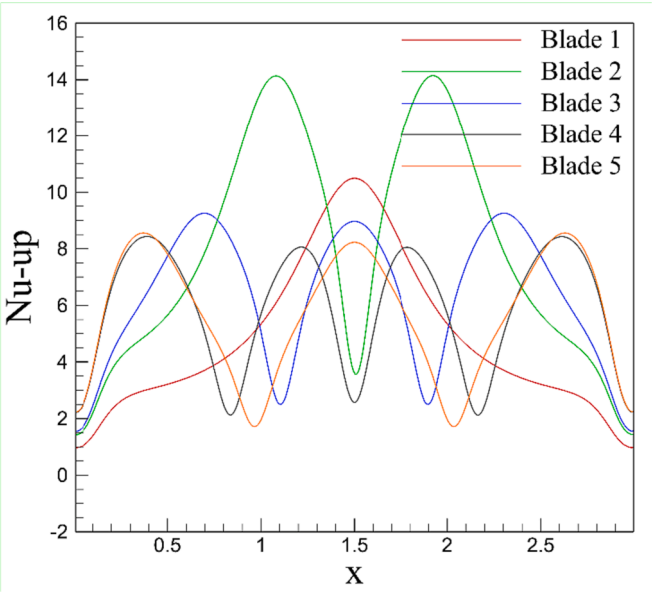

Fig. 9. Local Nu on the top wall for different N-Bs (1to5 blade) at Ra = 100000.

Table 4
Nu-Av on the top wall for two values of Ra (10^3 and 10^5) and different N-Bs (1to5 blade).

Blade	Ra = 10^3	Ra = 10^5
1	1.367	4.880
2	1.542	8.012
3	1.682	6.343
4	1.794	5.936
5	1.873	5.718

$$k_{nf} = \frac{k_p + 2k_f - 2(k_f - k_p)\varphi}{k_p + 2k_f + (k_f - k_p)\varphi} k_b + 5 \times 10^4 (8.4407)(100\varphi)^{-1.07304} \varphi \rho_f (C_p)_f \sqrt{\frac{k_b T}{\rho_p d_p} f(T,\varphi)} \quad (42)$$

$$f(T,\varphi) = \left(2.8217 \times 10^{-2}\varphi + 3.917 \times 10^{-3}\right)\left(\frac{T}{T_0}\right) + \left(-3.0669 \times 10^{-2}\varphi - 3.91123 \times 10^{-3}\right) \quad (43)$$

In the above equations, which represent viscosity and thermal conductivity, the effect of Brownian motion has been considered. In Table 2, the thermophysical properties of water and Al_2O_3 are shown. All parameters are calculated by substituting values from Table 2 for these properties.

Grid study and validation

It is very important to choose a suitable algorithm to solve the mentioned problem and achieve correct results. A FORTRAN code has been written to solve this problem. In this code, the initial parameters and the initial equilibrium distribution functions are considered. Then Equations (3) and (13), the equilibrium distribution function values are calculated in the fluid nodes, and Equations (1) and (12) are satisfied, and the new distribution function values (after collision) are calculated. After that, the flow stage is executed, where the values of the distribution functions of all the nodes are poured on the neighboring nodes in their own line. After applying the boundary conditions, the values of density, velocity and temperature in the entire network are calculated according to (Relations (6), 7 and 14) and if the results converge, the program ends, otherwise the described steps will be repeated.

Since experimental data is more accurate than numerical results, validation is done using experimental data to assess how accurate the current results are. For the validation, Krane and Jessee's experimental data [37] are employed. Fig. 4 presents a comparison between the horizontal velocity values in the cavity gained by the current study and the experimental data, indicating a remarkably high level of accuracy in the findings of this research.

In another validation, the maximum values of the vorticity power and average Nusselt number between the present work and Vahedi et al. [38] are compared in Table 3. Due to the triangular shape of the enclosure, this comparison has been conducted. The maximum error between the two results is 4.41 %.

The Nu-Av is calculated for various grid resolutions in order to conduct grid research (Fig. 5). 76,800 grid points are chosen for use in subsequent simulations based on the findings.

Results and discussion

Effect of Rayleigh number and n-bs

Fig. 6 illustrates the flow contours for two different values of Ra and the various N-Bs. It can be seen that the N-Bs has a direct effect on the number of vortices formed in such a way that the number of vortices formed in the cavity is increased with the N-Bs. For the case of 1 blade, two vortices with the opposite direction of rotation are formed in the cavity, which reaches 8 by increasing the N-Bs. The N-Bs and the Rayleigh number affect the vortices' strength and speed. An increment in the N-Bs causes the cavity to be divided into some parts and one or two vortices are formed in each part. The increase in the N-Bs causes the fluid to be in contact with a larger hot surface, and as a result, its temperature is enhanced more, leading to an enhancement in the strength of the vortex. An enhancement in the N-Bs leads to that less fluid occupying the cavity, reducing the vortex strength. At greater Rayleigh numbers, the vortices circulate more actively and create stronger vortices in different parts of the cavity. The increase of the buoyancy force causes the vortices in the cavity to move more swiftly.

The temperature contours for two distinct Ra values and the numerous N-Bs are shown in Fig. 7. The fluid travels towards the direction of the top wall in the regions where the isothermal lines are curving in that direction. The fluid also travels in the direction of the bottom wall in the regions where the isothermal lines are curving in that direction. It can be observed that the parts where the fluid is moving up and down are increased with the N-Bs. At Ra = 10^5, this is extremely clear. In the case of one blade, the fluid rises from the cavity's center and flows back down the side walls to the bottom wall. When there are two blades, the fluid flows up from the top of the two blades and then flows back down the side walls and through the cavity's center to the bottom wall. When there are three or four blades, the fluid travels from the tips of the blades to the top wall and from the sides of the insulated walls and the center of the blades to the bottom wall. When there are five blades, the fluid flows upward from the first, third, and fifth blades and downward from the second and fourth. At lower amounts of Ra, there are fewer isothermal lines in parallel, showing that the convection in the cavity is very low and the fluid has a very low velocity in the cavity. On the other hand, at higher Rayleigh numbers, isothermal lines are intertwined, indicating the nanofluid flow in the cavity.

Fig. 8 illustrates the local Nu on the top wall for different numbers of blades at Ra = 1000. The fluid flows slowly in the hollow as a result of the low Rayleigh number and buoyancy force, and there is little local nu on the low-temperature wall. The values of Nu on the beginning and end sections of the wall are lower than those in the intermediate regions of the wall for all various numbers of blades in the hollow. Due to the absence of flow penetration into the cavity's corner and the little temperature differential between the fluid and the wall in this area, the Nu is low. It can be seen that the local Nu s are higher in the parts where the

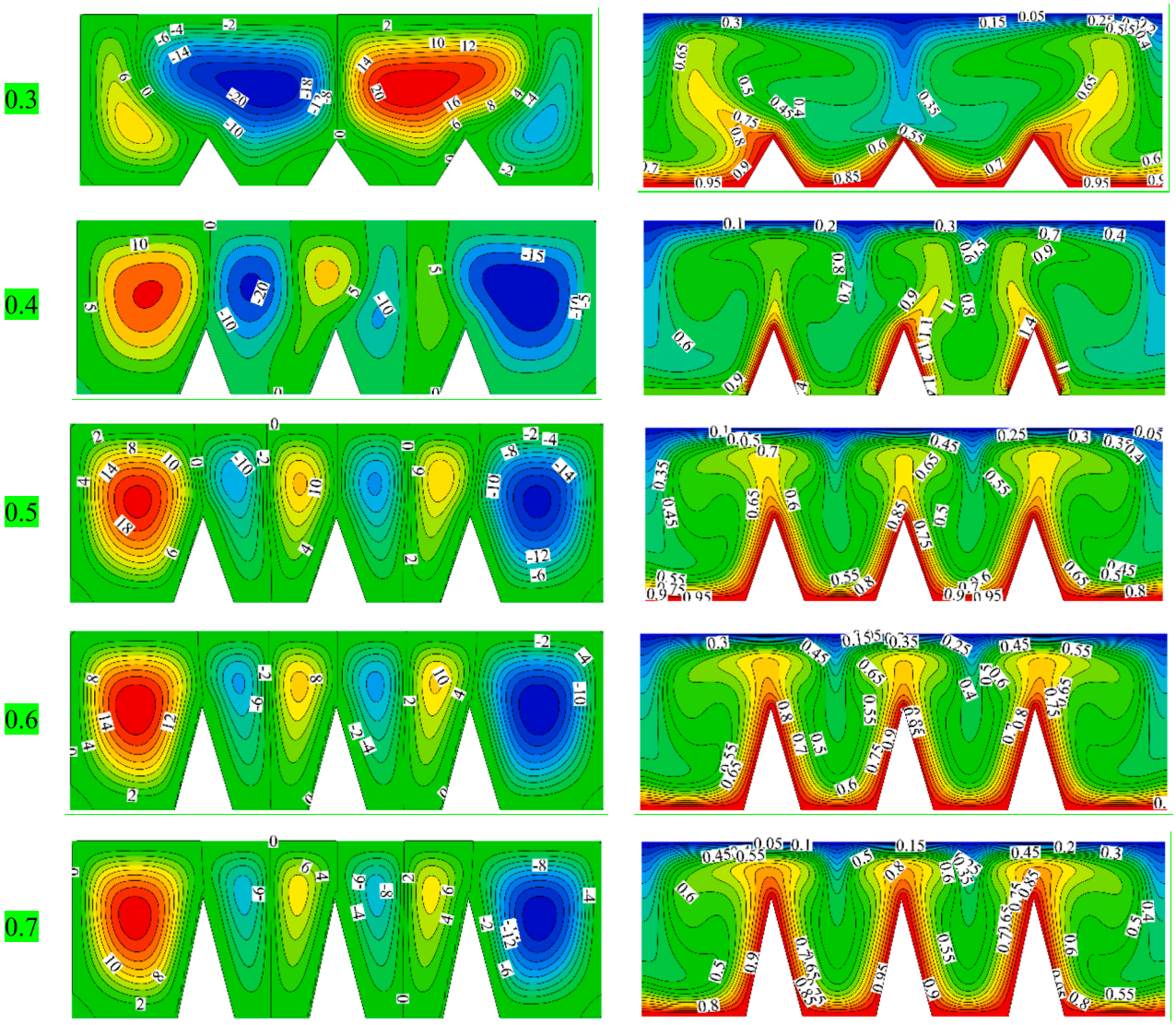

Fig. 10. Flow and temperature contours for different L-Bs from 0.3 to 0.7.

fluid meets the upper surface after coming into contact with the lower surface. These parts are observed as prominent peaks in the graph. Thus, the number of peaks is the same as the N-Bs. When the N-Bs is 5, the graph exhibits a noticeable peak because the blades have filled a significant portion of the cavity space, raising the temperature of the nanofluid and the local Nu.

Fig. 9 shows the local Nu on the top wall for different N-Bs at Ra = 100000. Comparing this figure with the previous one demonstrates that the enhancement in the Rayleigh number intensifies the local Nu in different parts, especially in the middle of the wall. The Nu increases on the wall because to the acceleration of the flow in the cavity and the increase in convection. Moreover, the higher and lower portions of the wall correspond to the minimum local Nu, as can be seen. It was justified by explanation. Additionally, when the fluid contacts the top wall from the side of the bottom wall, there is an extreme augmentation in the local Nu that is worse than the preceding figure. Particularly when the N-Bs in the cavity are 2, the local Nu concentration on the wall is excessively high. When the hot fluid contacts the cold wall or the cold fluid departs the wall and travels in the direction of the bottom wall, the velocity changes in the cavity are more evident at this level of Ra.

Table 4 provides the Nu-Av on the top wall for two values of Ra and different N-Bs. The value of the Nu on the wall with a low temperature rises when the Rayleigh number grows as a result of an increase in the fluid's velocity in the cavity and an increase in convection HTR. However, simultaneously increasing N-Bs in the cavity can both strengthen and weaken HTR on the low-temperature wall. The temperature of the nanofluid rises as a consequence of an increase in the heat exchange surface between the nanofluid and the high-temperature wall, which improves HTR. By increasing the number of N-Bs in the cavity, more space is taken up by them and less fluid is utilized in the cavity, which reduces the force required to move the fluid and transfer heat. Therefore, it is clear that the improvement in the N-Bs causes a rise in HTR at low Rayleigh numbers, where the relevance of convection is minimal. The N-Bs value of 5 results in the greatest degree of HTR. When the N-Bs is 2, the quantity of HTR is at its greatest at high Rayleigh numbers. HTR at high Rayleigh numbers is improved by the rise in N-Bs.

Effect of the l-bs

Fig. 10 demonstrates flow and temperature contours for different L-Bs from 0.3 to 0.7. Changing the L-B causes the strength of the vortex inside the cavity to reduce or enhance. Increases in the L-Bs lead to higher temperatures on high-temperature surfaces, higher fluid temperatures, and stronger buoyancy forces. But, an increase in the L-Bs causes a larger part of the cavity to be occupied by the blades. Hence, the space for the nanofluid is decreased and as a result, the convection

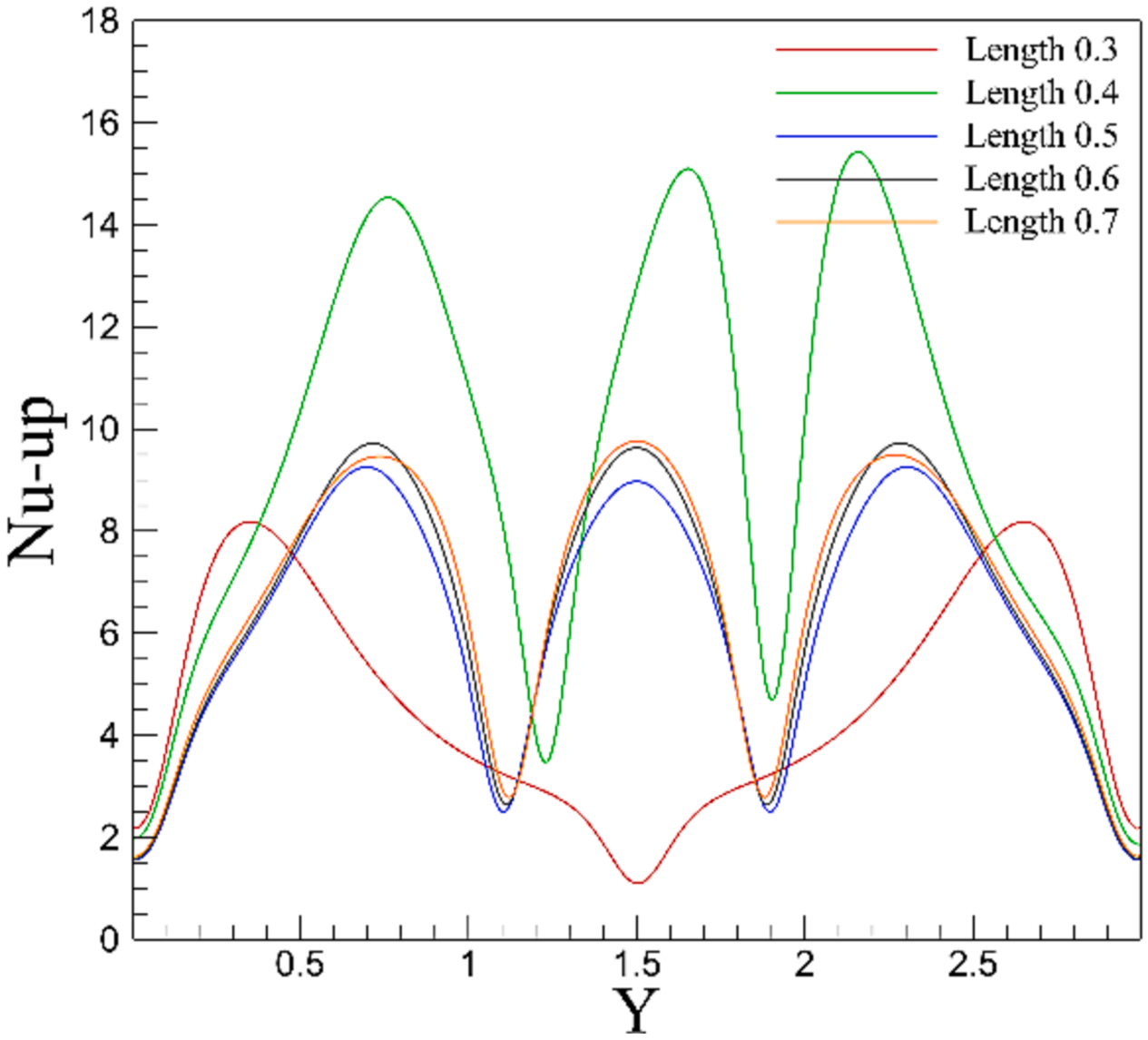

Fig. 11. Local Nu on the wall for different L-Bs of 0.3 to 0.7 at $10^{5.}$

Table 5
Nu-Av on the top wall for various L-Bs from 0.3 to 0.7 at $10^{5.}$

L	Num_{up}
0.3	4.7149
0.4	9.2569
0.5	6.3326
0.6	6.6629
0.7	6.8084

strength of the nanofluid is reduced. An increment in the L-Bs also affects the number of vortices formed in the cavity. It can be seen that with an enhancement in the L-B from 0.3 to 0.5, the shape and number of vortices formed in the cavity change. However, the shape and number of vortices do not change significantly by increasing the L-B from 0.5 to 0.7. It is evident that the isothermal lines differ in shape as a result of the nanofluid's motion toward the cavity's top or bottom walls. For the L-Bs of 0.3 and 0.4, it can be seen that the place where the nanofluid rises is different and sometimes it moves diagonally towards the sides of the wall. However, for the L-Bs of 0.5 to 0.7, the nanofluid moves upward from the top of the blades, the surfaces of the thermally insulated walls, and the spacing between the blades.

Fig. 11 displays the local Nu on the wall for different L-Bs ranging from 0.3 to 0.7. All blade lengths, with the exception of 0.3, have three peaks in the images, which correspond to the three points on the wall where the hot fluid meets the cold wall. When the L-B is 0.3, two pieces of the hot fluid collide with the low-temperature wall. The local Nu is at its highest point at L-B = 0.4. Because to the low temperature differential and less fluid penetration in such regions, the lowest Nu is found at the beginning and end of the wall. Since the height of the blades causes a decrease in the fluid velocity, the enhancement in their length does not intensify the local Nu at a distance of 0.75, 1.5, and 2.25 from the low-temperature wall. The minimum local Nusselt wall occurs when the L-B is 0.3, which takes place in the middle of the wall, and its value is less than 2.

The Nu-Av on the top wall for various L-Bs ranging from 0.3 to 0.7 is shown in Table 5. An increase in the L-Bs improves the fluid's contact surface with the hot wall, which raises the temperature of the nanofluid and, in turn, improves HTR between the nanofluid and the cold wall. However, increasing the L-Bs results in the blades taking up more space and using less nanofluid in the cavity, which reduces the motion of the

nanofluid in the cavity. When the L-B is 0.4, the Nu-Av reaches its maximum value. A further rise in L-Bs results in a significant reduction in Nu-Av. The L-B must be 0.3 to get the lowest Nu-Av. As can be observed, increasing the L-Bs from 0.3 to 0.4 increases the average Nusselt by more than 96 % when the L-B is on the low-temperature wall.

Conclusions

This article investigates the effects of employing various geometrical features of triangular blades inserted in a sealed compartment on a nanofluid's natural convection HTR when a magnetic field is present. The effect of using triangular blades on the hot wall and employing different heights of blades from 0.3 to 0.7 are evaluated at two amounts of Ra. The following results are obtained.

1- The maximum amount of local Nu occurs on the low-temperature wall when the blade number is 3 and the L-B changes from 0.4 to 0.7.
2- The boost in the N-Bs increases HTR when Ra $= 10^3$, where the convection is feeble; the greatest HTR occurs when the N-Bs is 5.
3- When the N-Bs is 2, the HTR is at its greatest when Ra $= 10^5$. The N-Bs continue to rise, but the HTR decreases.
4- When the L-B is 0.4, the Nu-Av reaches its maximum value. The Nu significantly decreases as the L-B continues to rise.
5- By raising the L-Bs from 0.3 to 0.4, the Nu-Av on the low-temperature wall is raised by more than 96 %.
6- Increasing the Reynolds number results in a more powerful generation of the flow field and greater coherence of streamlines.

Author statement

The authors confirm their contribution to the paper as follows: Data curation, J. Mustafa, A.M. Alsaiari; Investigation, S. Alqaed and J. Mustafa; Methodology, S. Alqaed, S. M. Sajadi and Hikmet S. Aybar; Project administration, J. Mustafa and S. M. Sajadi.; Writing—original draft, j. mustafa, Hikmet S. Aybar; Writing— review and editing, J. Mustafa, S. Alqaed and Hikmet S. Aybar. All authors reviewed the results and approved the final version of the manuscript.

CRediT authorship contribution statement

Jawed Mustafa: Writing – review & editing, Writing – original draft, Project administration, Investigation, Data curation. **Saeed Alqaed:** Writing – review & editing, Methodology, Investigation. **S. Mohammad Sajadi:** Project administration, Methodology. **Abdulrahman Mohammed Alsaiari:** Data curation. **Hikmet Ş. Aybar:** Writing – review & editing, Writing – original draft, Methodology.

Declaration of competing interest

The authors declare that they have no known competing financial interests or personal relationships that could have appeared to influence the work reported in this paper.

Data availability

No data was used for the research described in the article.

Acknowledgment

The authors are thankful to the Deanship of Scientific Research at Najran University for funding this work under the Future Funding program grant code (NU/SRP/SERC/12/20).

References

[1] Miroshnichenko I, Sheremet M. Turbulent natural convection heat transfer in rectangular enclosures using experimental and numerical approaches: A review. Renew Sustain Energy Rev 2018;82:40–59.
[2] Patankar SV. Numerical heat transfer and fluid flow. CRC Press; 2018.
[3] Khan ZH, Khan WA, Hamid M, Liu H. Finite element analysis of hybrid nanofluid flow and heat transfer in a split lid-driven square cavity with Y-shaped obstacle. Phys Fluids 2020;32.
[4] Zhao X, Yang Z, Meng X, Wang S, Li R, Xu H, et al. Study on Mechanism and Verification of Columnar Penetration Grouting of Time-Varying Newtonian Fluids 2023;11:1151.
[5] Mustafa J, Abdullah MM, Ahmad MZ, Jamil B, Sharifpur M. Frictional, thermal, and total entropy generation of two-phase nanofluid turbulent flow in a circular heatsink: A numerical study. Eng Anal Bound Elem 2023;150:44–55.
[6] Khan ZH, Khan WA, Yang Z, Hamid M, Qasim M. Mixed convection flow in a channel with a dimpled section and adiabatic cylindrical obstacle under the influence of magnetic and Joule effects. Results Phys 2023;49:106550.
[7] Murthy, J. Y., S. R. Mathur, Computational heat transfer in complex systems: a review of needs and opportunities, 2012.
[8] Perumal DA, Dass AK. A Review on the development of lattice Boltzmann computation of macro fluid flows and heat transfer. Alex Eng J 2015;54:955–71.
[9] Li Q, Luo KH, Kang Q, He Y, Chen Q, Liu Q. Lattice Boltzmann methods for multiphase flow and phase-change heat transfer. Prog Energy Combust Sci 2016;52:62–105.
[10] He Y-L, Liu Q, Li Q, Tao W-Q. Lattice Boltzmann methods for single-phase and solid-liquid phase-change heat transfer in porous media: A review. Int J Heat Mass Transf 2019;129:160–97.
[11] Alqaed S, Mustafa J, Almehmadi FA, Alharthi MA, Elattar HF, Refaey HA, et al. Entropy generation of the laminar and mixed flow of alumina/water nanofluid flow in a two-dimensional rectangular enclosure affected by a magnetic field using the lattice Boltzmann method. Eng Anal Bound Elem 2023;151:187–98.
[12] Aidun CK, Clausen JR. Lattice-Boltzmann method for complex flows. Annu Rev Fluid Mech 2010;42:439–72.
[13] Martys NS, Chen H. Simulation of multicomponent fluids in complex three-dimensional geometries by the lattice Boltzmann method. Phys Rev E 1996;53:743.
[14] Raabe D. Overview of the lattice Boltzmann method for nano-and microscale fluid dynamics in materials science and engineering. Model Simul Mater Sci Eng 2004;12:R13.
[15] Lai T, Liu X, Chu J, He M, Zhang Y. Numerical Study of Flow and Heat Transfer in a Rectangular Channel Partially Filled with Porous Media at the Pore Scale Using Lattice Boltzmann Method. Heat Transfer Eng 2022;43:818–29.
[16] Zhang X, Xu Y, Zhang J, Rahmani A, Sajadi SM, Zarringhalam M, et al. Numerical study of mixed convection of nanofluid inside an inlet/outlet inclined cavity under the effect of Brownian motion using Lattice Boltzmann Method (LBM). Int Commun Heat Mass Transfer 2021;126:105428.
[17] Yuki JQ, Sen I, Sakib MMQ, Nag P, Molla MM. Multiple-relaxation-time lattice Boltzmann simulation of magnetic field effect on natural convection of non-Newtonian nanofluid in rectangular enclosure. Advances in Applied Mathematics and Mechanics 2021;13:1142–68.
[18] Di Ilio G, Ubertini S, Succi S, Falcucci G. Nanofluid Heat Transfer in Wavy-Wall Channels with Different Geometries: A Finite-Volume Lattice Boltzmann Study. J Sci Comput 2020;83:56.
[19] Khan ZH, Makinde OD, Usman M, Ahmad R, Khan WA, Huang Z. Inherent irreversibility in unsteady magnetohydrodynamic nanofluid flow past a slippery permeable vertical plate with fractional-order derivative. J Comput Des Eng 2023;10:2049–64.
[20] Maji A, Choubey G. Improvement of heat transfer through fins: A brief review of recent developments. Heat Transfer 2020;49:1658–85.
[21] Kraus AD, Aziz A, Welty J, Sekulic D. Extended surface heat transfer. Appl Mech Rev 2001;54:B92–.
[22] Razelos P. A critical review of extended surface heat transfer. Heat Transfer Eng 2003;24:11–28.
[23] Abu-Nada E, Chamkha AJ. Mixed convection flow of a nanofluid in a lid-driven cavity with a wavy wall. Int Commun Heat Mass Transfer 2014;57:36–47.
[24] Khan ZH, Akbar NS, Akram J, Hamid M, Wei Y. Electroosmotically Augmented Peristaltic Flow of Carbon Nanotubes Based Nanofluid through Asymmetrical Channel 2023;103:e202100354.
[25] Alqaed S, Mustafa J, Sharifpur M. Numerical investigation and optimization of natural convection and entropy generation of alumina/H2O nanofluid in a rectangular cavity in the presence of a magnetic field with artificial neural networks. Eng Anal Bound Elem 2022;140:507–18.
[26] Jun Song Z, Khan ZH, Ahmad R, Khan WA, Wei Y. Thermal analysis of ferromagnetic nanofluid flow in a channel over a dimpled cavity. J Magn Magn Mater 2023;573:170653.
[27] Kao PH, Yang RJ. Simulating oscillatory flows in Rayleigh-Bénard convection using the lattice Boltzmann method. Int J Heat Mass Transf 2007;50:3315–28.
[28] Chen S, Doolen GD. Lattice Boltzmann method for fluid flows. Annu Rev Fluid Mech 1998;30:329–64.
[29] Guo Z, Zheng C, Shi B. Discrete lattice effects on the forcing term in the lattice Boltzmann method. Phys Rev E 2002;65:046308.
[30] Mei R, Luo L-S, Shyy W. An accurate curved boundary treatment in the lattice Boltzmann method. J Comput Phys 1999;155:307–30.
[31] Guo Z, Zheng C, Shi B. An extrapolation method for boundary conditions in lattice Boltzmann method. Phys Fluids 2002;14:2007–10.

[32] Xuan Y, Roetzel W. Conceptions for heat transfer correlation of nanofluids. Int J Heat Mass Transf 2000;43:3701–7.
[33] Brinkman H. The viscosity of concentrated suspensions and solutions. J Chem Phys 1952;20:571.
[34] Hamilton RL, Crosser O. Thermal conductivity of heterogeneous two-component systems. Ind Eng Chem Fundam 1962;1:187–91.
[35] Vajjha RS, Das DK. Experimental determination of thermal conductivity of three nanofluids and development of new correlations. Int J Heat Mass Transf 2009;52:4675–82.
[36] Pordanjani AH, Jahanbakhshi A, Nadooshan AA, Afrand M. Effect of two isothermal obstacles on the natural convection of nanofluid in the presence of magnetic field inside an enclosure with sinusoidal wall temperature distribution. Int J Heat Mass Transf 2018;121:565–78.
[37] Krane, R. J., Jessee, J, Some detailed field measurements for a natural convection flow in a vertical square enclosure, In Proceedings of the First ASME-JSME Thermal Engineering Joint Conference, 1, 323-329, 1983.
[38] Vahedi SM, Aghakhani S, Pordanjani AH, Azaiez J. A comprehensive parametric study on heat transfer optimization of a triangular enclosure subjected to a magnetic field using neural network machine learning. Eng Anal Bound Elem 2022;145:173–86.